Optical Engineering

OpticalEngineering.SPIEDigitalLibrary.org

# Dual-polarization airborne lidar for freshwater fisheries management and research

Michael R. Roddewig
Nathan J. Pust
James H. Churnside
Joseph A. Shaw

SPIE.

Michael R. Roddewig, Nathan J. Pust, James H. Churnside, Joseph A. Shaw, "Dual-polarization airborne lidar for freshwater fisheries management and research," *Opt. Eng.* **56**(3), 031221 (2017), doi: 10.1117/1.OE.56.3.031221.

# Dual-polarization airborne lidar for freshwater fisheries management and research

**Michael R. Roddewig,[a] Nathan J. Pust,[a] James H. Churnside,[b] and Joseph A. Shaw[a,*]**
[a]Montana State University, Electrical and Computer Engineering Department, Bozeman, Montana, United States
[b]National Oceanic and Atmospheric Administration, Earth Systems Research Laboratory, Boulder, Colorado, United States

**Abstract.** The design of a compact, dual-polarization, nonscanning lidar system intended to fly in a small, single-engine aircraft for airborne study of freshwater marine ecosystems and mapping of fish schools in mountain lakes is discussed. Design trade-offs are presented with special attention paid to selecting the field of view and telescope aperture diameter. Example results and a comparison with a similar existing lidar system are presented.  [DOI: 10.1117/1.OE.56.3.031221]

Keywords: lidar; remote sensing; limnology; fisheries; water optics.

Paper 161201SS received Jul. 28, 2016; accepted for publication Feb. 1, 2017; published online Mar. 1, 2017.

## 1 Introduction

Airborne lidar study of freshwater ecosystems is still a relatively unexplored field, and there are many applications in lake and river ecology, fisheries, and so forth.[1] Multiple airborne bathymetric lidar systems have been developed for looking into seawater, primarily for profiling the seafloor surface and, sometimes, also for measuring the optical properties of the water column.[2–8] Lidars also have been developed for airborne or shipborne measurements of water clarity and attenuation,[9–11] spatial and temporal variations in oceanic scattering layers and plankton distributions,[12–14] internal waves,[15] chlorophyll content,[16–18] and fish.[19] Recently, a space-based lidar was used for producing global maps of phytoplankton biomass and total particulate organic carbon.[20] These lidars rely on elastic scattering, although Brillouin scattering has been investigated as a method for lidar profiling of water temperature.[21–25]

These previous studies focused almost exclusively on oceanic measurements, with comparatively little study in freshwater. The purpose of this paper is to describe the design of a low-cost, compact, nonscanning lidar system for freshwater lake studies from a single-engine airplane. This instrument was developed to explore the potential for lidar study of freshwater lakes throughout Montana and the Greater Yellowstone Ecosystem. Many simplifications were made to reduce the cost by more than an order of magnitude relative to high-performance bathymetric lidar instruments. The two initial scientific objectives for this instrument were the mapping of invasive lake trout (*Salvelinus namaycush*) spawning sites in Yellowstone Lake and other waters and large-scale mapping of plankton layers.

Fisheries biologists at Yellowstone National Park have been attempting to eliminate a population of invasive lake trout in Yellowstone Lake for over a decade.[26,27] This invasive species threatens the integrity of the Yellowstone Ecosystem. The National Park Service's primary method of removing lake trout from the lake is via gill-netting from boats, and gill-netting at the spawning sites of these trout is particularly successful.[28] Locating these spawning sites is therefore of great importance.[29]

We also wanted to design a lidar that would be able to map plankton layers in freshwater lakes. Characterizing the spatial extent of plankton layers in freshwater lakes has been the subject of recent research, but these studies have either been conducted from the surface with sampling limited to either transects or selected locations,[30,31] or have relied on moderate-resolution imaging spectroradiometer data, which has limited spatial resolution with a 1-km pixel size.[32,33] Airborne lidar has the potential to augment the detailed data that can be obtained on the surface with high-resolution, large-scale maps of these plankton layers.

## 2 System Design

Cost was a driving design requirement and shaped many of the design decisions we made. This lidar was intended to cost under $100,000 USD and be flown in small, single-engine aircraft, such as the Cessna 185, to minimize operating costs. Penetration to large depths was not a requirement because during the spawning season lake trout are at depths of just a few meters,[29,34] and data from local lakes indicated plankton rarely existed in great numbers beyond 15 m.[35]

A major feature of this lidar was the ability to make measurements of both the co- and cross-polarized signals and thus measure the depolarization ratio. Fish, zooplankton, and phytoplankton all depolarize lidar signals to varying extents, and measuring the amount of depolarization can provide useful information.[1]

In the following sections, we discuss some of the design decisions we made for various parts of the lidar system. The first sections discuss the optical design, covering choice of laser, field of view (FOV), and aperture size, and then moving onto coaxial versus separate receivers for each polarization, and the lidar tilt angle. We then cover the more interesting aspects of the electronics and software design, and conclude with example data and a comparison with the National Oceanic and Atmospheric Administration (NOAA) Fish Lidar, which performs similar work in the ocean.

*Address all correspondence to: Joseph A. Shaw, E-mail: joseph.shaw@montana.edu.

### 2.1 *Laser Selection*

Important considerations for laser selection are the wavelength, divergence, and the pulse length and repetition frequency. The most common wavelength for marine lidar is 532 nm, owing to the wide availability of rugged, small, and inexpensive lasers, and favorable absorption characteristics in natural waters. While the absorption of light in pure water has a minimum at ~420 nm,[36] the absorption minimum shifts to longer wavelengths as the concentration of dissolved organic matter increases.[1,37] Morel[38] developed a model that related the chlorophyll concentration to the attenuation coefficient of downwelling irradiance, $K_d$, which showed that at chlorophyll concentrations above ~0.2 mg/m$^3$ the attenuation at 500 nm is less than that at 400 nm. Chlorophyll-a concentrations are well above this level in Flathead Lake[39] and Yellowstone Lake,[40] especially during the summer months. For these reasons, we chose 532 nm as our design wavelength.

The laser pulse width creates a limit on the accuracy of depth information that can be obtained by the lidar. For our fisheries application, we simply need to detect the presence of fish and possibly quantify the biomass of the fish present in a given area.[41] We are not able to distinguish fish species; suspected lake trout spawning sites are identified by consideration of the location and depth of the detected fish in concert with other ecological parameters in a manner similar to what is used with acoustical tracking devices.[28,42] In this case, the loss of precision due to a large pulse width is not an impediment. When profiling plankton layers, precise measurements of depth are more useful, but these measurements can be easily obtained from the surface. Thus, while short pulse width was important, it was not a major requirement.

The pulse repetition frequency (PRF) limits the maximum speed that the aircraft can travel while maintaining overlap between adjacent shots and must be high enough to allow for a reasonable flight speed if continuous coverage along the flight path is desired. Thought must also be given to the laser divergence as it is desirable to match the divergence and the FOV of the receiver. Broadening a narrow laser beam is often easily accomplished with a negative lens.

Based on previous positive experiences with Big Sky Laser products, we chose the air-cooled, diode-pumped, 40 mJ Centurion laser (Quantel, Bozeman, Montana). This laser is similarly robust to lasers we have used in the past and is diode-pumped, which provides better electrical efficiency. The Centurion outputs a 40-mJ pulse at 1064 nm, which is doubled to 532 nm. Any residual energy at 1064 nm is blocked. Pulse energy at 532 nm is 26 mJ, output divergence is 5 mrad, pulse length is 7.2 ns, and maximum PRF is 100 Hz. Our pulse-limited depth resolution is 80 cm in water, and with an 800 mega-samples per second (MSPS) digitizer, the sample-rate limited depth resolution in water is 14 cm.

### 2.2 *Received Signal and Background Power*

FOV and receiver aperture size are crucial considerations as the product of aperture area and FOV projected solid angle gives the radiometric throughput for an optical receiver.[43] A wide FOV will reduce the effective attenuation in water by capturing multiply scattered photons but will increase the amount of unwanted background light received. To help choose these parameters, we modeled the signal-to-noise ratio (SNR) and signal-to-background ratio (SBR) for various FOV and receiver aperture sizes.

The received electrical lidar signal power $P_{\text{electrical}}(z)$ in watts at depth $z$ is calculated similarly to Churnside[1]

$$P_{\text{electrical}}(z) = \left[\frac{E_0 A T_S^2 \eta n v}{2(nH+z)^2}\beta(\pi, z)e^{-2\alpha z}\right]^2 R_L, \quad (1)$$

where $E_0$ is the laser pulse energy, $A$ is the receiver aperture area, $T_S$ is the surface transmission, $\eta$ is the photomultiplier tube (PMT) responsivity, $n$ is the water index of refraction, $v$ is the speed of light in vacuum, $H$ is the plane altitude, $\beta(\pi, z)$ is the volume scattering coefficient at angle pi radians, assumed to be constant over depth, $\alpha$ is the lidar attenuation coefficient and is discussed below, and other parameters are given in Table 1. The laser divergence and receiver FOV are assumed to be matched and in full overlap, and for this simple model, we ignored the effect of polarization and the transmission of the optics. For our lidar, we used a PMT receiver, which directly drives the digitizer.

The water surface is assumed to be flat and the reflection at the surface is computed using the Fresnel equations for the lidar tilt angle. The value obtained for the surface transmission of $T_S = 0.951$ for this simple model does not differ significantly from a rigorous computation by Mobley[45] for a polarized sky and various wind speeds.

The lidar attenuation coefficient $\alpha$ is an "effective" attenuation coefficient, which accounts for the effects of multiple scattering in the water. The following equation is from

**Table 1** Lidar parameters to model received signal, SNR, and SBR for various fields of view and receiver aperture sizes. Laser parameters are from the Quantel Centurion laser. Digitizer parameters are for the GaGe CS148001U USB Digitizer. PMT parameters are for the Hamamatsu H7680. Parameters not used in the simulation are unlisted.

| | | |
|---|---|---|
| **Laser** | Wavelength | 532 nm |
| | Pulse width $\tau_p$ | 7.2 ns |
| | Pulse energy $E_0$ | 26 mJ |
| **Digitizer** | Voltage step size $\delta_V$ | 134 $\mu$V |
| | Bandwidth $B$ | 700 MHz |
| **PMT** | Anode responsivity $\eta$ (at 2.5-V gain voltage) | 440 A/W |
| | Dark current $I_D$ | 200 nA |
| **Other** | Load resistance $R_L$ | 50 Ω |
| | Lidar tilt angle | 15 deg |
| | Filter bandwidth $B_f$ | 2 nm |
| | Water index of refraction $n$ | 1.333 |
| | Altitude $H$ | 300 m |
| | Single-scatter albedo[44] | 0.85 |

Churnside,[1] which was derived from Monte Carlo simulations of oceanic lidar by Gordon:[46]

$$\alpha = K_d + (c - K_d)e^{-0.85cD}, \tag{2}$$

where $D$ is the lidar spot diameter on the water surface, $c$ is the beam attenuation coefficient, and $K_d$ is the diffuse attenuation coefficient. This effective attenuation coefficient accounts for the FOV loss that results from scattering in the water.[47,48]

By definition, $c = a + b$, where $a$ is the attenuation coefficient and $b$ is the scattering coefficient. Measurements of optical properties of local lakes are lacking, so for simulation we were forced to estimate these parameters. Models from Gallie and Murtha[49] were used to estimate $a$ and $b$ given chlorophyll-a concentration, suspended mineral concentration, and colored dissolved organic matter (CDOM, referred to as "yellow substance" by Gallie). The chlorophyll-a concentration of 0.75 $\mu$g/L is a representative number from Yellowstone Lake[40] while the suspended mineral concentration of 3 mg/L and CDOM value of 0.3 $m^{-1}$ (at 350 nm) are numbers from Chilko Lake,[49] an oligotrophic lake in British Columbia similar to Yellowstone Lake, as these data were unavailable for local lakes. These values yielded $a = 0.179$ $m^{-1}$ and $b = 0.8427$ $m^{-1}$ at 540 nm. Thus, for simulation, the beam attenuation coefficient $c = 1.0214$ $m^{-1}$.

To compute the diffuse attenuation coefficient, we used the equation from Lee et al.[50]

$$K_d = a + 4.18b_b \cdot [1 + 0.52e^{-10.8a}], \tag{3}$$

where $b_b$ is the backscattering coefficient. To calculate $b_b$, we integrated the phase scattering function values listed by Mobley[51] with the calculated total scattering coefficient $b$ from above to yield $b_b = 0.0153$ $m^{-1}$. Thus, $K_d = 0.2474$ $m^{-1}$. This result was verified using a different expression from Phillips and Kirk that yielded an estimate for $K_d$ of 0.2655 $m^{-1}$.[52]

To determine the volume scattering coefficient $\beta(\pi;\lambda)$, we used the definition of the spectral volume scattering phase function $\tilde{\beta}(\phi;\lambda)$, where $\tilde{\beta}(\phi;\lambda) \cdot b(\lambda) = \beta(\phi;\lambda)$. The value of the phase scattering function is again taken from Mobley,[51] $\tilde{\beta}(\pi; 530\text{ nm}) = 3.154 \cdot 10^{-3}$ $sr^{-1}$, which yields $\beta(\pi; \sim 532\text{ nm}) = 3.9 \cdot 10^{-3}$ $m^{-1}$ $sr^{-1}$.

In computing the SNR, we took into account shot and ideal quantization noise. Shot noise power is defined as $P_{\text{shot noise}} = 2qIBR_L$, where $q$ is the elementary charge, $I$ is the output current of the PMT (including the background signal and dark current), $B$ is the system bandwidth, and $R_L$ is the load resistance.[53] The quantization noise power is defined as $P_{\text{quantization noise}} = \delta_V^2/12$, where $\delta_V$ is the digitizer voltage step size. Thus, SNR is computed in dB as (expressed in decibels)

$$\text{SNR}_{\text{dB}} = 10 \cdot \log_{10}\left(\frac{P_{\text{electrical}}}{P_{\text{shot noise}} + P_{\text{quantization noise}}}\right), \tag{4}$$

and SBR is computed as (in decibels)

$$\text{SBR}_{\text{dB}} = 10 \cdot \log_{10}\left(\frac{P_{\text{electrical}}}{P_{\text{background}} + P_{\text{dark current}}}\right), \tag{5}$$

where $P_{\text{dark current}} = I_D^2 R_L$. $P_{\text{background}} = L_B A \Omega_{\text{FOV}} B_f$, where $\Omega_{\text{FOV}}$ is the receiver FOV solid angle and $B_f$ is the filter bandwidth, which is given in Table 1. $L_B$ is the background radiance, which was computed to be 100 mW $m^{-2}$ $sr^{-1}$ $nm^{-1}$ using moderate-resolution atmospheric transmission for a standard rural atmosphere with 5-km visibility at Yellowstone Lake.

### 2.3 *Effects of Varying Receiver Aperture Diameter and Field of View*

To determine an optimal receiver configuration, we modeled the effects of varying the receiver aperture diameter and FOV. We first tested aperture diameters from 5 to 15 cm for a 5-mrad FOV, which matches the unexpanded laser beam divergence. The results are shown in Fig. 1. Increasing receiver aperture size improves the SNR (by increasing the received signal power), although because of our high background radiance the lidar remains SBR-limited in all configurations. With less background light, the simulation indicates that for a 5-mrad FOV a 15-cm-diameter telescope is optimal, with maximum depth of penetration at 13 m; however, the gains to be had by increasing aperture diameter are quite modest, especially given the expense of a larger aperture and the difficulty of fitting a large telescope in a small airplane. The results for a 15-mrad FOV are similar to those for the 5-mrad FOV.

The same plots were generated for 10-, 15-, and 20-mrad fields of view for a 5-cm-diameter aperture (shown in Fig. 2) and follow the same pattern as increasing the aperture size, but with slightly larger improvements in penetration depth compared to the aperture diameter case. Each configuration is again SBR-limited, although increasing the FOV has improved the performance relative to increasing the aperture diameter. Again considering only the SNR, the simulation indicates that a 5-cm-diameter aperture with a 10-mrad FOV outperforms the 15-cm-diameter aperture with a narrower 5-mrad FOV. These plots demonstrate the importance of the FOV in capturing multiply scattered photons as was noted by Gordon.[46]

Figure 3 shows the effects of varying the aperture diameter and FOV on the received power from 5, 7.5, and 10 m in depth, again emphasizing the advantage of increasing the FOV versus increasing the aperture diameter.

Eye safety is an important part of FOV calculations. The single pulse exposure limit is 5 mJ/$m^2$.[54] Because it is possible for a stationary observer to view two pulses as the plane passes overhead, we apply a correction factor of $N_p^{-0.25}$, where $N_p = 2$ is the number of pulses,[1] yielding an eye safety limit of 4.21 mJ/$m^2$. For our laser, the pulse energy is 26.8 mJ and our nominal flight altitude is 300 m. Without expansion, the laser beam divergence is 5 mrad, which gives a spot area of 1.75 $m^2$ on the water surface and a laser energy of 15 mJ/$m^2$, above the eye safety limit calculated above; however, expanding the beam to 15 mrad yields a laser energy of 1.7 mJ/$m^2$, below the calculated limit.

Our instrument operates at a 5- and 15-mrad FOV, with matched laser divergences. The narrow FOV is used to study the lidar attenuation coefficient in water as it more closely approximates the beam attenuation coefficient.[46] The wide FOV is used to study fish and plankton because of its greater depth penetration. Section 2.7 discusses the precautions we

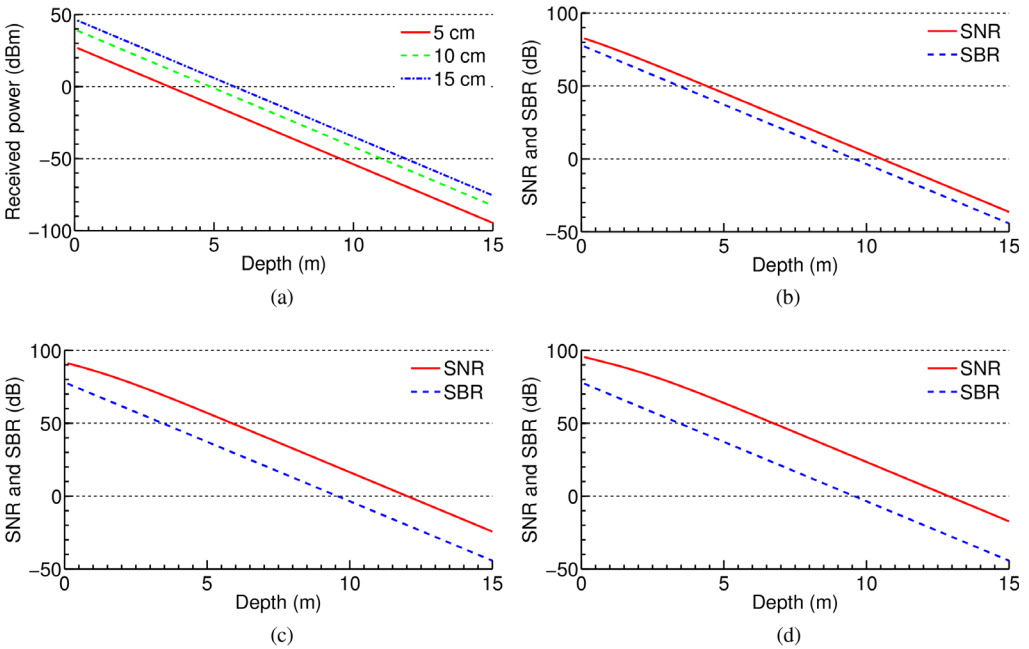


**Fig. 1** Received power (a) and SNR and SBR for a 5-, 10-, and 15-cm-diameter aperture and 5-mrad FOV [parts (b), (c), and (d), respectively]. Increasing the aperture diameter provides modest improvements in SNR, although the lidar remains SBR-limited in each case.

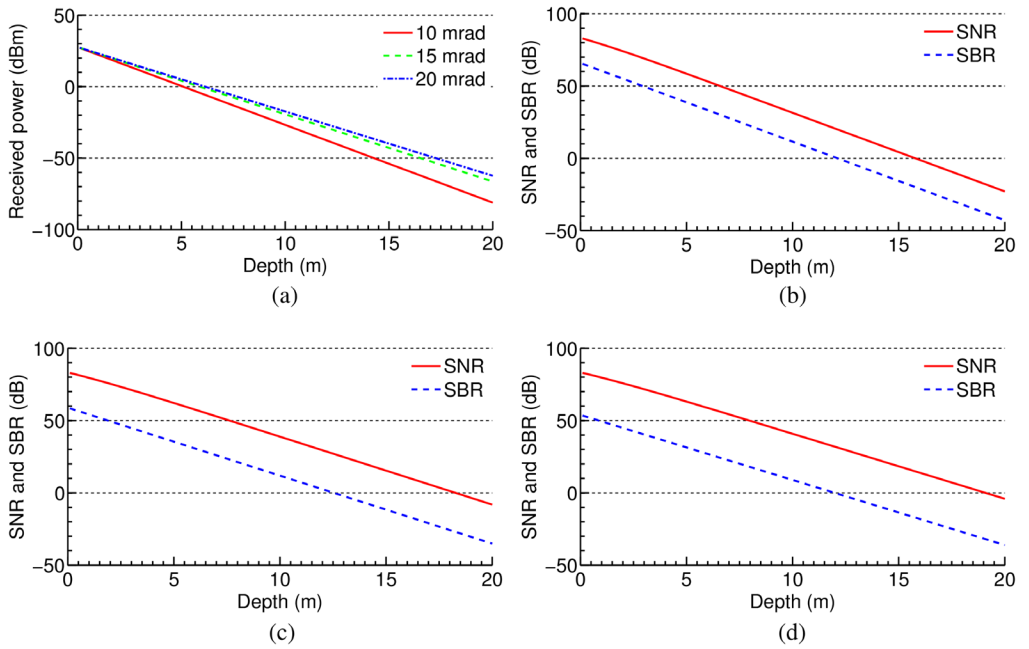


**Fig. 2** Received power (a) and SNR and SBR for a 5-cm-diameter telescope and 10-, 15-, and 20-mrad FOVs [parts (b), (c), and (d), respectively]. Increasing the FOV limits the loss from multiply scattered light.

take in the narrow FOV configuration when the laser beam is not eye safe.

### 2.4 *Signal-to-Noise Ratio and Signal-to-Background Ratio for Lake Trout*

We wanted to verify that the lidar would be able to detect spawning lake trout in local lakes. During the several week spawning season in the fall, lake trout congregate in large groups at spawning sites close to the surface, at depths of just a few meters. Preferred spawning sites are rocky shoals, devoid of vegetation, and the fish will habitually return to the same site each year.[55–61] This behavior is the key that allows lidar to locate their spawning sites and is also why knowledge of the location of their spawning sites is of such importance in controlling their population.

Churnside[41] performed a detailed study of the lidar backscatter from sardines and developed equations to compute

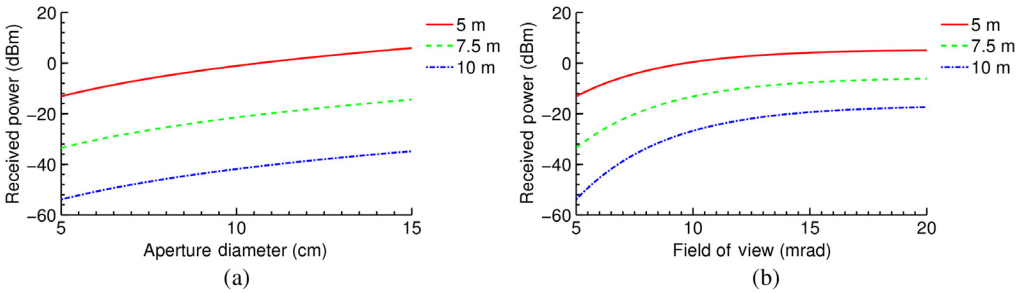


**Fig. 3** Received power at 5-, 7.5-, and 10-m depth for (a) 5- to 15-cm aperture diameter and 5-mrad FOV and (b) 5- to 20-mrad FOV and 5-cm aperture diameter.

the cross-sectional area $A_f$ and volume backscatter coefficient at angle pi $\beta_f$ of fish, which we use here to model the lidar signal from a lake trout.

For lake trout, we chose a Lambertian reflectivity $\rho = 0.146$, which is a worst-case number for ocean fish as similar data for freshwater fish are unavailable.[62] 53 cm was chosen for the length, which is a representative number from Yellowstone Lake.[27] Using the model from Churnside, we computed $\beta_f = 0.0016\ \mathrm{m^{-1}\ sr^{-1}}$. The lidar signal is again computed using Eq. (1) with $\beta_f$ substituted for $\beta(\pi, z)$.

SNR was defined as

$$\mathrm{SNR_{dB}} = 10 \cdot \log_{10}\left(\frac{P_{\mathrm{fish}}}{P_{\mathrm{shot\ noise}} + P_{\mathrm{quantization\ noise}}}\right), \tag{6}$$

where $P_{\mathrm{fish}}$ is the power reflected from the fish. SBR was defined as

$$\mathrm{SBR_{dB}} = 10 \cdot \log_{10}\left(\frac{P_{\mathrm{fish}}}{P_{\mathrm{background}} + P_{\mathrm{dark\ current}}}\right). \tag{7}$$

Other parameters were the same as in Table 1. The results for a 5-cm-diameter telescope and 5- and 15-mrad FOVs are displayed in Fig. 4, which again demonstrate the advantages of increasing the FOV.

### 2.5 *Coaxial Receivers*

Many dual-polarization lidars use a single optical assembly with some method of separating polarizations, either with a polarizing beamsplitter cube, liquid crystal variable retarder,[63] or other method of discriminating co- and cross-polarization.

We chose to use separate co- and cross-polarization receivers mounted side by side. Optically, this makes the receivers simpler but increases the difficulty of aligning and calibrating the lidar. Because of this, alignment is performed on the ground at a test range, and calibration is performed in a lab. Alignment while in the air is not feasible due to variations in the signal from the water surface and because the small size of the plane makes it difficult to adjust the lidar while in flight. This raises the concern of the lidar losing alignment during flight and being unable to correct it; however, this has yet to happen.

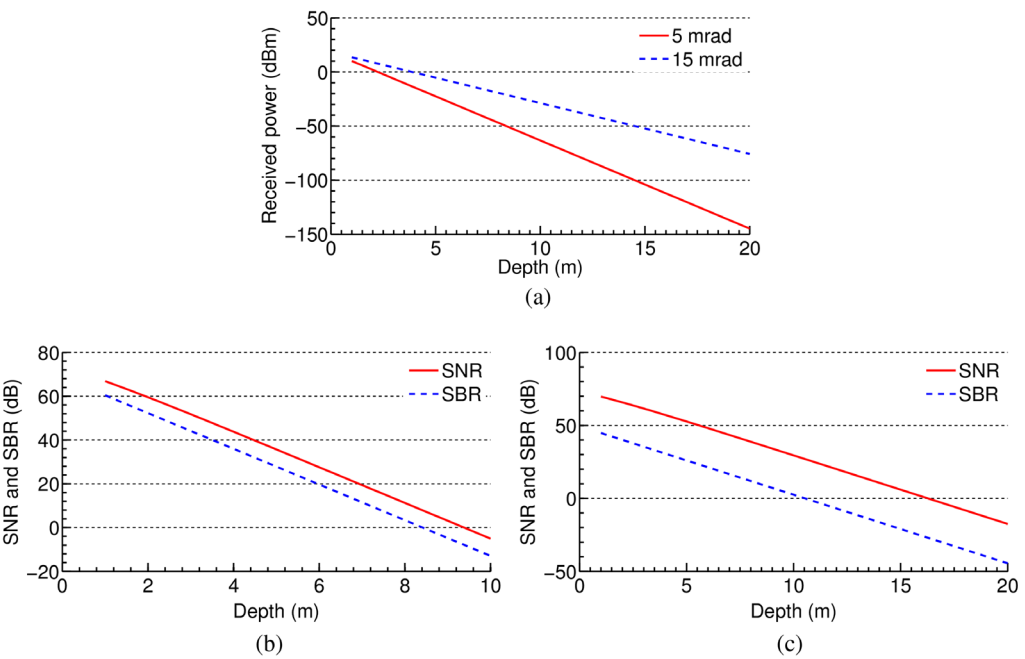


**Fig. 4** Received power (a) and SNR and SBR plots for a single lake trout, 5-cm-diameter telescope, and 5- and 15-mrad FOVs [parts (b) and (c), respectively].

Each receiver is calibrated separately using an integrating sphere so we are able to make meaningful comparisons between the co- and cross-polarized signal. The sphere is cycled through a series of radiance values, and at each value, the PMT output is recorded as the PMT gain voltage is varied. We then calculate a fit to a $4 \times 1$ calibration polynomial, given below

$$L_e = p_{00} + p_{10}g + p_{01}y + p_{20}g^2 + p_{11}gy + p_{30}g^3 + p_{21}g^2y + p_{40}g^4 + p_{31}g^3y, \quad (8)$$

where $L_e$ is the radiance measured in $\mathrm{W\,cm^{-2}\,sr^{-1}\,nm^{-1}}$, $g$ is the PMT gain in volts, $y$ is the PMT output in volts, and $p_{xx}$ are the calibration gains. This model fits the wide FOV receiver responses better, with $R^2 > 0.9$ for each channel. The fit to the narrow FOV receivers is not as good, with $R^2 > 0.7$. This appears to stem from the light output from the integrating sphere being too weak at lower PMT gain values.

### 2.6 *Tilt Angle*

Marine lidars are typically operated at a small angle from zenith to reduce the unwanted specular reflection from the water surface, which is often very large and can saturate the copolarized receiver. To determine the optimum tilt angle, we performed a simple simulation where we considered the laser as a single ray pointed at the surface (without divergence). Using the calibration discussed in the previous section, we computed the amount of light at each receiver necessary to saturate the digitizer. We then calculated $\phi_{\mathrm{sat}}$, how far in radians outside the FOV $\phi_{\mathrm{FOV}}$ the laser beam could fall while saturating the receivers.

To model the distribution of wave slope angles, we used the Gram Charlier distribution from Cox and Munk.[64] Shaw and Churnside[65] showed that the Cox and Munk distribution is valid for near-neutral conditions (i.e., equal air and water temperatures), but that it underestimates surface roughness with negative stability (water warmer than air). We assumed the worst-case scenario where the receiver tilt is aligned w ith the wind direction. $\sigma_u^2$ was calculated using the "clean surface" equations, as were the skewness and peakedness coefficients. We then computed the probability that a wave slope falls within the saturation angle

$$\theta_{\mathrm{sat}} = \theta_{\mathrm{lidar\ tilt}} \pm (\phi_{\mathrm{FOV}} + \phi_{\mathrm{sat}}), \quad (9)$$

where $\theta_{\mathrm{lidar\ tilt}}$ was the lidar head tilt angle. This probability was then used in a binomial experiment to determine the probability of saturation in a given time period, assuming the lidar is run at 50 shots per second (the typical repetition rate in practice). Results are shown in Fig. 5 for wind speeds from 1 to 20 m/s and lidar tilt angles from 5 to 30 deg.

From the simulation, we chose 15 deg as our lidar tilt angle, but the system was designed so that this angle is adjustable. Increasing the angle beyond 15 deg would lessen the probability of saturation but could possibly eliminate the surface return altogether, in which case our surface detection algorithm would fail. At a 5-m/s wind speed and 4-V gain voltage, the probability of the copolarized receiver not saturating in 5 min is 0.94 (min/max radiance is 0.02 and 710 $\mathrm{W\,cm^{-2}\,sr^{-1}\,nm^{-1}}$, respectively) and the probability of the cross-polarized receiver at a 3.5-V gain voltage

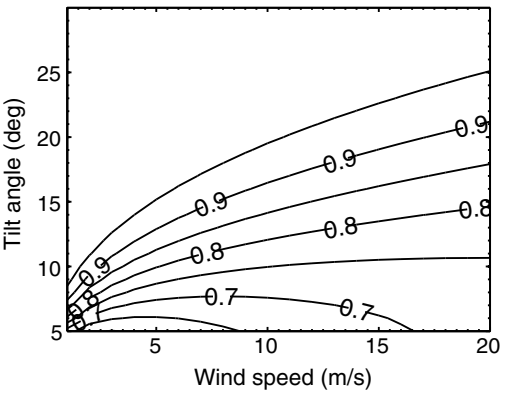


**Fig. 5** The probability of the copolarized receiver at 4-V gain voltage not saturating in 5 min at wind speeds from 1 to 20 m/s and tilt angles from 5 deg to 30 deg. In the final design, we chose 15 deg as our tilt angle.

not saturating is 0.91 (min/max radiance is 0.02 and 465 $\mathrm{W\,cm^{-2}\,sr^{-1}\,nm^{-1}}$, respectively), which was acceptable for our purposes. We have not experienced significant problems with saturation at 15 deg in practice. Due to safety concerns, we do not fly if surface wind speeds exceed 7 m/s.

### 2.7 *Final Optical Design*

Initially, the lidar was designed with a 5-cm-diameter copolarized aperture and 5-mrad "narrow" FOV (e.g., undiverged laser beam). The cross-polarized aperture diameter was increased to 7.5 cm to better capture the typically weaker cross-polarized signal. After simulation and field studies proved the narrow FOV was inadequate, the capability to operate at a "wide" 15-mrad FOV was added. This is achieved by placing a negative diverging lens in front of the laser and changing out the receiver telescopes. The optical system was designed so that this can be accomplished without adjusting the alignment, and calibrations are performed for both FOVs. A FOV "swap" can be performed on the ground in ~30 min.

Because the narrow-FOV configuration is not eye safe it is not operated near people or animals. During most flights, this does not present a significant impediment, as the lakes we study are remote and typically have little to no human activity. During flight, the pilot constantly monitors for people/animals and other hazards on the surface, which are easily identified and avoided because of the low flight altitude. These precautions are not necessary for the wide-FOV configuration.

The current system is not scanned, and the receivers and laser are held in a fixed orientation to the plane. This first system was intended as a proof-of-concept to investigate the possibility of studying freshwater ecosystems with lidar. Adding a scanner system would increase the complexity, cost, and size of the system but could be useful in the future.

### 2.8 *Dynamic Range and Digitizer Considerations*

Dynamic range is an important consideration in lidar design. Older designs typically used either a logarithmic amplifier or two separate digitizers to achieve an acceptable dynamic range as high-speed digitizers were limited to eight bits. Designs using logarithmic amplifiers suffer from the challenge of calibrating the amplifiers and large quantization

noise for larger signals. Using multiple digitizers also requires careful calibration and attention to matching the phase, frequency, and amplitude responses of each digitizer.

Modern digitizers are just becoming available with high sample rates and larger bit depths. For our project, we chose to use a GaGe CS148001U 14-bit, 800 MSPS USB digitizer from GaGe Applied (Lachine, Quebec, Canada). This digitizer has an ideal dynamic range of 86 dB, but when the effective number of bits (ENOB) is considered the actual dynamic range is only 69 dB, corresponding to an ENOB of 11.2, which provides penetration depth to close to the SNR-limit of the 5-cm-diameter aperture, 15-mrad FOV optical design.

### 2.9 *Trigger Generation, Computer Interface, and Power Supply*

A custom-built trigger generator using a Xilinx (San Jose, California) Spartan-6 field-programmable gate array (FPGA) allowed a USB-programmable variable delay to gate the PMTs and trigger the digitizers. Careful attention was paid during FPGA design to ensure a worst-case timing skew between trigger outputs of 171 ps. A 64-MHz clock frequency provides a delay resolution (in air) of 4.7 m, with a minimum delay of 65 m. Because the trigger delay is programmable, we minimize extraneous data captured by the lidar and enable it to be easily adjusted for different flight altitudes.

All the hardware was designed to interface with the computer via USB, and the entire lidar was controlled from a laptop with one USB cable. This minimizes the amount of cabling in the aircraft cabin and simplified installation. We have, however, experienced some difficulties with the limited data bandwidth of USB 2.0. If the laser was operated at the full 100 Hz PRF, we missed lidar shots because the samples could not be transferred quickly enough to the computer. To avoid this, the laser was operated at a reduced 50 Hz PRF, which still provides sufficient shot overlap at a 44-m/s flight speed. Upgrading to USB 3.0 would solve this problem and allow us to fly at a greater speed, but USB 3.0 digitizers were not available when the system was designed. Figure 6 is a block diagram that illustrates the major electronic components of the lidar system.

Despite the higher electrical efficiency of the diode-pumped laser the power requirements for our lidar still exceed what has been available from our small planes. To power the lidar, we used a 12-V, 92 AH deep-cycle battery and a 600-W, pure sine-wave, regulated AC inverter. This configuration was able to power the lidar while collecting data for ∼2 h.

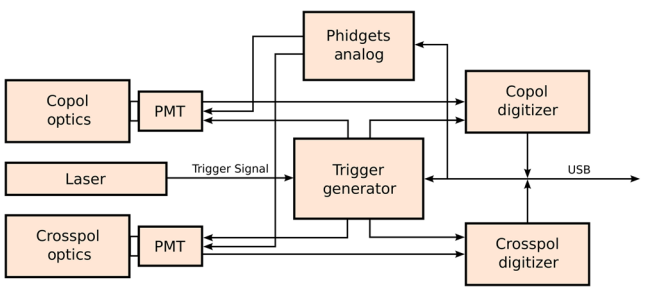


**Fig. 6** Block diagram of the major electronic components of the lidar system.

### 2.10 *Synchronization*

A major task was synchronizing each piece of hardware and software because each component was designed to operate asynchronously. The digitizers were synchronized to each other using an Abracon SYNC-10 portable 10 MHz frequency reference (Irvine, California) and a −3-dB splitter, with matched cables feeding each digitizer.

The computer was synchronized to global positioning system (GPS) time using a Time Machines TM1000A GPS Time Server (Lincoln, Nebraska). Each incoming piece of data was then timestamped by the computer as it arrived so that it could later be matched with the corresponding GPS location.

To synchronize the digitizers to the computer time, a feature of the GaGe digitizers was enabled that timestamped each shot from a given "epoch," which is set by the computer. Each shot could then be associated with a matching shot from the other digitizer and timestamped by the computer.

### 2.11 *Operating Software Design*

The software is divided into two major pieces: the application software, which runs the lidar in the air, and the post-processing software, which generates the images for analysis after a flight.

The application software allows the operator to troubleshoot errors and monitor the operation of the lidar during flight but does not perform any analysis of the data. During the hardware selection, we took note of the programming libraries available for each component and selected C#.NET as the development language for this software program as all the hardware had libraries in this language.

The software enables the operator to adjust the laser PRF, PMT gains, and trigger altitude. Both single shots and an "echosound" plot are displayed, as well as the laser status, temperature, and the GPS location.

Data were stored on the fly in a SQLite database. SQLite was chosen over a "flat-file" storage scheme due to the ease of programmatic access and implementation, with minimal overhead. The application stored the raw data, PMT gains, trigger altitude, and the time for each shot. Laser PRF, sample rate, and laser head tilt angle along with remarks for each run were stored in a separate configuration table. A third table stored the calibration parameters; however, data were not stored calibrated to prevent a mistake in the calibration parameters from ruining data from a run. Each shot had a cross-reference to the related entry in the configuration and calibration table. GPS data were stored in a separate table with both a computer and GPS timestamp, to guard against errors in either corrupting a data run and for comparison.

### 2.12 *Postprocessing Software Design*

After completing a lidar run, the data stored in the database were processed using a Python application that converted the digital number to radiance, calculated the exact location and altitude of each shot, and also computed the location of the water surface and the depth increment for each sample.

The water surface was identified using a basic algorithm that located the maximum signal peak in the copolarized channel and then walked "backward" in the direction of the lidar to 1% of this maximum value, which we called the "surface." While this algorithm may fail when the surface return

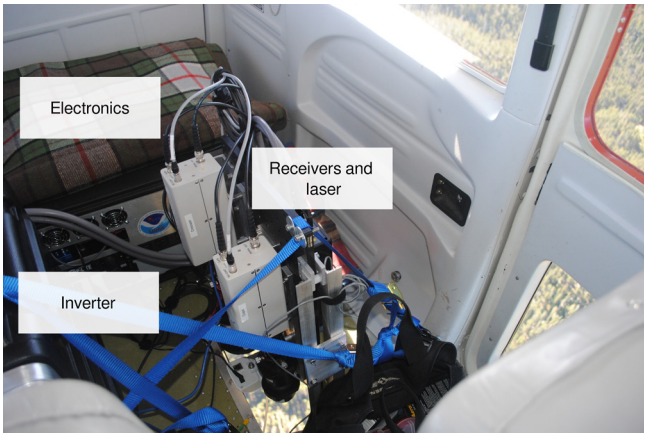


**Fig. 7** The lidar mounted in the plane. The lidar optics are mounted over a hole in the floor of the plane and tilted forward at an angle of 15 deg to reduce the surface reflection. Behind the lidar head is the electronics case and to the left in the photo is the inverter case.

is weaker than the volumetric scattering from the water immediately below the surface,[66] our lidar is not intended to perform high-accuracy bathymetry, and a low-cost solution was preferable to other proposed solutions to this problem, such as a separate infrared or Raman channel requiring an extra receiver and associated hardware.[2] This is a capability that could be added in the future by unblocking the 1064-nm output of the laser.

Each shot location was calculated using coordinates from a commercial GPS receiver with wide area augmentation system capability. The location of shots taken between position fixes was interpolated.

Shots were assembled into false-color images, an example of which is shown in Fig. 10 in Sec. 4. These images were examined qualitatively for the presence of fish or plankton; no automated algorithms to detect these organisms in freshwater are known by us to currently exist.[67]

## 3 Comparison to the NOAA Fish Lidar

Churnside[13,15,19,68] has developed an airborne lidar for oceanic ecosystem studies, the "NOAA Fish Lidar." This lidar shares many similarities with the lidar that we described here and was the basis for our design. A 532-nm flash-pumped Nd:YAG laser is used, which produces 12 ns, 100 mJ pulses at a PRF of 30 Hz. The copolarized receiver aperture diameter is 6 cm, and the cross-polarized receiver aperture diameter is 15 cm. FOV is 16 mrad, slightly larger than the 15 mrad wide FOV of our lidar. Over the years, the NOAA lidar has evolved to incorporate two receivers to measure both co- and cross-polarized radiation and has been reduced in size to where it can be flown in a four-seat Cessna 177, very similar to the Cessna 185 in which our lidar operates.[15]

There are some differences between the two. Our lidar uses a diode-pumped laser for its higher electrical efficiency and shorter pulse width. This laser has a lower pulse energy but is able to operate at a higher PRF (up to 100 Hz). The NOAA lidar uses a logarithmic amplifier paired with a 1-GSPS, 8-bit digitizer to achieve a dynamic range of ~40 dB. Because of the larger bit depth of our digitizers, we are able to directly sample the lidar signal without the need for an intermediate logarithmic amplifier and achieve a larger 69 dB dynamic range. This simplifies the overall system.

The NOAA system uses an embedded high-speed computer to digitize and process the data, which allows the use of PCI-Express (PCIe) digitizers. This avoids the problems we have encountered with USB digitizers, which we are limited to because we designed our entire lidar system to be run off a single laptop. PCIe digitizers are numerous whereas high-speed USB digitizers are still fairly rare. We may move to PCIe digitizers in the future to get around the USB bandwidth bottleneck.

## 4 Experimental Results

The lidar we have described has been successfully flown over Flathead Lake in Montana, Yellowstone Lake in Yellowstone National Park, and several other local lakes in Montana. Figure 7 shows the lidar mounted in the rear of a Cessna 185. Potential lake trout spawning sites are qualitatively identified by the authors through examination of the data. Prior work where lidar data were compared with echosounder data has shown that fish typically appear as long spikes because of the long laser pulse.[19,41,69,70] Potential spawning sites are identified by considering the location and depth of the fish. No automated algorithms for freshwater fish identification currently exist, and this is an area for future research.

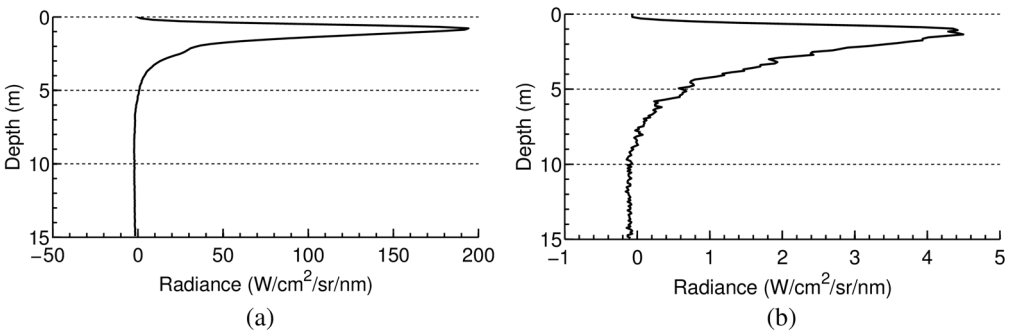


**Fig. 8** A representative single lidar shot from Yellowstone Lake in clear water without the presence of fish or a shallow lake bottom. The copolarized trace is plotted in (a) and the cross-polarized trace in (b). The maximum of the surface pulse appears at ~1 m in depth because the surface detection algorithm locates this maximum and then finds the point on the pulse toward the surface where the power is 1% of this maximum, which is the first part of the laser pulse reflected from the surface.

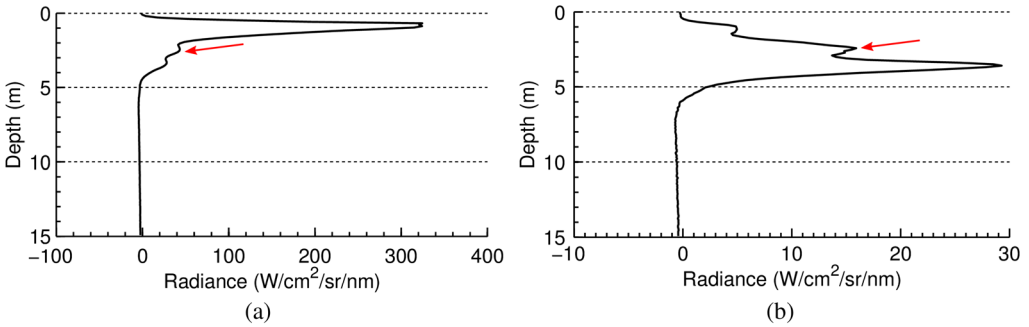


**Fig. 9** An example single lidar shot from Yellowstone Lake showing a return typical of fish and a shallow lake bottom. The copolarized trace is plotted in (a) and the cross-polarized trace in (b). The fish appear as the bump at ~2.5 m highlighted by the red arrow; the lake bottom is just below at ~4 m.

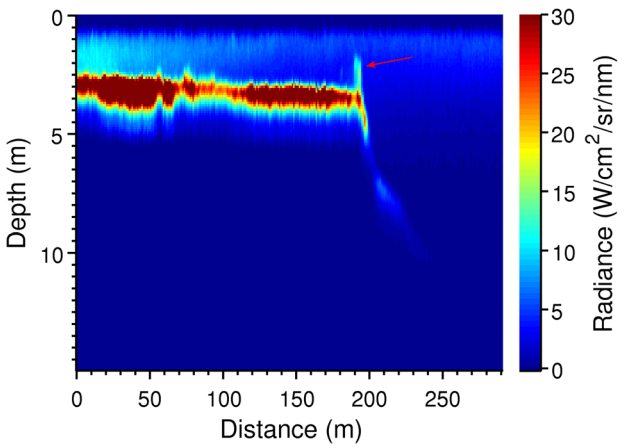


**Fig. 10** An image from the cross-polarized channel of the fish return depicted in Fig. 9 in Yellowstone Lake. The fish are indicated by the red arrow.

Figure 8 shows an example lidar shot from Yellowstone Lake in clear water. The return from the water usually falls below the receiver noise at about 10 m in the cross-polarized trace, which is fairly close to the 12 m predicted in simulation. The optical properties used to develop the SNR and SBR simulations had to be estimated or were measurements taken from similar bodies of water. Often, the only optical properties available for a given lake are Secchi disk depths, which are rough estimates of the water optical properties.[71,72] Measurement of local freshwater lake trophic and optical properties may reduce this discrepancy as assuming parameters from other lakes is problematic; Kirk notes that estimates for the absorption coefficient of CDOM vary widely, even for lakes in the same general area.[73]

Figure 9 shows an example single lidar shot with the presence of fish from Yellowstone Lake, and Fig. 10 shows an image from the cross-polarized channel of the same fish hit.

## 5 Conclusion

In this article, we discussed the design and implementation of an airborne lidar for freshwater ecosystem studies, including the rationale behind some of the choices we made in the optical, electronic, and software designs. SNR and SBR plots for various aperture and FOV sizes were presented. Dynamic range is often a limiting factor in lidar designs, and it is important to consider the real-world dynamic range of a given digitizer (using the ENOB) and not the theoretical dynamic range. With the advent of digitizers with high bit-rate and bit-depth, older approaches for increasing limited digitizer dynamic range may no longer be necessary.

Our lidar system uses two receivers, which necessitated a more complicated calibration but was a simpler and less expensive approach. Alignment is more difficult, but we have not yet encountered any major difficulties.

The biggest limitation of our instrument during these initial experiments was the limited data bandwidth of USB 2.0. Moving to USB 3.0 digitizers would allow us to run at a higher PRF, as currently we have to limit the PRF to avoid missing shots. We are also considering moving the processing and digitizers to an embedded computer system, which would allow us to use PCIe digitizers.

Since finishing construction, we have completed successful flights of Yellowstone Lake, Flathead Lake, and other lakes throughout Montana.

## Acknowledgments

The development of this instrument was supported by the Montana Institute on Ecosystems award from National Science Foundation (NSF) EPSCoR Track-1 under Grant No. NSF-IIA-1443108. Any opinions, findings, and conclusions, or recommendations expressed in this material are those of the author(s) and do not necessarily reflect the views of the NSF. Additional support was provided by the Montana Research and Economic Development Initiative and the Montana Space Grant Consortium.

## References

1. J. H. Churnside, "Review of profiling oceanographic lidar," *Opt. Eng.* **53**(5), 051405 (2014).
2. G. C. Guenther, R. W. Thomas, and P. E. LaRocque, "Design considerations for achieving high accuracy with the shoals bathymetric lidar system," *Proc. SPIE* **2964**, 54–71 (1996).
3. W. J. Lillycrop, L. E. Parson, and J. L. Irish, "Development and operation of the shoals airborne lidar hydrographic survey system," *Proc. SPIE* **2964**, 26–37 (1996).
4. G. H. Tuell et al., "Measurement of ocean water optical properties and seafloor reflectance with scanning hydrographic operational airborne lidar survey (SHOALS): II. Practical results and comparison with independent data," *Proc. SPIE* **5885**, 58850E (2005).
5. P. E. LaRocque, J. R. Banic, and A. G. Cunningham, "Design description and field testing of the SHOALS-1000T airborne bathymeter," *Proc. SPIE* **5412**, 162 (2004).
6. V. Ramnath et al., "Predicted bathymetric lidar performance of coastal zone mapping and imaging lidar (CZMIL)," *Proc. SPIE* **7695**, 769511 (2010).
7. G. Tuell, K. Barbor, and J. Wozencraft, "Overview of the coastal zone mapping and imaging lidar (CZMIL): a new multisensor airborne

mapping system for the us army corps of engineers," *Proc. SPIE* **7695**, 76950R (2010).
8. B. D. Reineman et al., "A portable airborne scanning lidar system for ocean and coastal applications," *J. Atmos. Oceanic Technol.* **26**(12), 2626–2641 (2009).
9. J. H. Churnside, V. V. Tatarskii, and J. J. Wilson, "Oceanographic lidar attenuation coefficients and signal fluctuations measured from a ship in the Southern California Bight," *Appl. Opt.* **37**(15), 3105–3112 (1998).
10. D. M. Allocca et al., "Ocean water clarity measurement using shipboard lidar systems," *Proc. SPIE* **4488**, 106–114 (2002).
11. C. San Lin, "Ocean lidar instrument and measurements," *Proc. SPIE* **4880**, 127 (2003).
12. A. P. Vasilkov et al., "Airborne polarized lidar detection of scattering layers in the ocean," *Appl. Opt.* **40**(24), 4353–4364 (2001).
13. J. H. Churnside and P. L. Donaghay, "Thin scattering layers observed by airborne lidar," *ICES J. Marine Sci.: J. Cons.* **66**(4), 778–789 (2009).
14. O. A. Bukin et al., "Measurement of the lightscattering layers structure and detection of the dynamic processes in the upper ocean layer by shipborne lidar," *Int. J. Remote Sens.* **19**(4), 707–715 (1998).
15. J. H. Churnside et al., "Airborne lidar detection and characterization of internal waves in a shallow fjord," *J. Appl. Remote Sens.* **6**(1), 063611 (2012).
16. K. J. Lee et al., "Helicopter-based lidar system for monitoring the upper ocean and terrain surface," *Appl. Opt.* **41**(3), 401–406 (2002).
17. A. M. Chekalyuk et al., "New technological developments for ocean lidar biomonitoring," *Proc. SPIE* **5155**, 22 (2003).
18. M. Kampel et al., "Simultaneous measurements of chlorophyll concentration by lidar, fluorometry, above-water radiometry, and ocean color MODIS images in the southwestern Atlantic," *Sensors* **9**(1), 528–541 (2009).
19. J. H. Churnside, V. V. Tatarskii, and J. J. Wilson, "Airborne lidar for fisheries applications," *Opt. Eng.* **40**(3), 406–414 (2001).
20. M. J. Behrenfeld et al., "Space-based lidar measurements of global ocean carbon stocks," *Geophys. Res. Lett.* **40**, 4355–4360 (2013).
21. D. J. Collins et al., "Recent progress in the measurement of temperature and salinity by optical scattering," *Proc. SPIE* **0489**, 247–269 (1984).
22. E. S. Fry et al., "Accuracy limitations on Brillouin lidar measurements of temperature and sound speed in the ocean," *Appl. Opt.* **36**(27), 6887–6894 (1997).
23. A. Popescu, K. Schorstein, and T. Walther, "A novel approach to a Brillouin–lidar for remote sensing of the ocean temperature," *Appl. Phys. B: Lasers Opt.* **79**(8), 955–961 (2004).
24. K. Schorstein, E. S. Fry, and T. Walther, "Depth-resolved temperature measurements of water using the Brillouin lidar technique," *Appl. Phys. B* **97**, 931–934 (2009).
25. A. Rudolf and T. Walther, "Laboratory demonstration of a Brillouin lidar to remotely measure temperature profiles of the ocean," *Opt. Eng.* **53**(5), 051407 (2014).
26. L. R. Kaeding, G. D. Boltz, and D. G. Carty, "Lake trout discovered in Yellowstone Lake threaten native cutthroat trout," *Fisheries* **21**(3), 16–20 (1996).
27. T. M. Koel et al., "Nonnative lake trout result in Yellowstone cutthroat trout decline and impacts to bears and anglers," *Fisheries* **30**(11), 10–19 (2005).
28. R. E. Gresswell et al., "Identifying movement patterns and spawning areas of invasive lake trout *Salvelinus namaycush* in Yellowstone Lake," Technical Report, US Geological Survey, Northern Rocky Mountain Science Center, Bozeman, Montana (2012).
29. P. E. Bigelow, "Predicting areas of lake trout spawning habitat within Yellowstone Lake, Wyoming," PhD Thesis, University of Wyoming (2009).
30. T. Mehner, F. Holker, and P. Kasprzak, "Spatial and temporal heterogeneity of trophic variables in a deep lake as reflected by repeated singular samplings," *Oikos* **108**, 401–409 (2005).
31. K. Rinke et al., "Lake-wide distributions of temperature, phytoplankton, zooplankton, and fish in the pelagic zone of a large lake," *Limnol. Oceanogr.* **54**(4), 1306–1322 (2009).
32. N. Bergamino et al., "Spatio-temporal dynamics of phytoplankton and primary production in Lake Tanganyika using a MODIS based bio-optical time series," *Remote Sens. Environ.* **114**(4), 772–780 (2010).
33. L. S. Cardoso et al., *Hydrodynamics—Natural Water Bodies*, Intech, Rijeka, Croatia (2012).
34. D. L. Perkins and C. C. Krueger, "Dynamics of reproduction by hatchery-origin lake trout (*Salvelinus namaycush*) at Stony Island Reef, Lake Ontario," *J. Great Lakes Res.* **21**, 400–417 (1995).
35. S. J. Interlandi, S. S. Kilham, and E. C. Theriot, "Responses of phytoplankton to varied resource availability in large lakes of the greater Yellowstone ecosystem," *Limnol. Oceanogr.* **44**(3), 668–682 (1999).
36. F. M. Sogandares and E. S. Fry, "Absorption spectrum (340–640 nm) of pure water. I. photothermal measurements," *Appl. Opt.* **36**(33), 8699–8709 (1997).
37. C. D. Mobley, *Light and Water: Radiative Transfer in Natural Waters*, Academic Press, San Diego, California(1994).
38. A. Morel, "Light and marine photosynthesis: a spectral model with geochemical and climatological implications," *Prog. Oceanogr.* **26**(3), 263–306 (1991).
39. B. K. Ellis, Alternate states in a large oligotrophic lake: a retrospective analysis of nutrient loading and food web change," PhD Thesis, University of Montana, Missoula, Montana (2007).
40. L. M. Tronstad et al., "Introduced lake trout produced a four-level trophic cascade in Yellowstone Lake," *Trans. Am. Fish. Soc.* **139**(5), 1536–1550 (2010).
41. J. H. Churnside, K. Sawada, and T. Okumura, "A comparison of airborne lidar and echo sounder performance in fisheries," *J. Marine Acoust. Soc. Jpn.* **28**(3), 175–187 (2001).
42. B. S. Cox, "Assessment of an invasive lake trout population in Swan Lake, Montana," Master's Thesis, Montana State University-Bozeman, College of Letters & Science (2010).
43. J. A. Shaw, "Radiometry and the Friis transmission equation," *Am. J. Phys* **81**(1), 33–37 (2013).
44. R. P. Bukata et al., "Determination of inherent optical properties of Lake Ontario coastal waters," *Appl. Opt.* **18**(23), 3926–3932 (1979).
45. C. D. Mobley, "Polarized reflectance and transmittance properties of windblown sea surfaces," *Appl. Opt.* **54**(15), 4828–4849 (2015).
46. H. R. Gordon, "Interpretation of airborne oceanic lidar: effects of multiple scattering," *Appl. Opt.* **21**(16), 2996–3001 (1982).
47. L. C. Bobb, G. Ferguson, and M. Rankin, "Laser irradiance in the sea: theory and experiment," Technical Report, DTIC, Fort Belvoir, Virginia (1978).
48. G. C. Guenther, "Airborne laser hydrography: system design and performance factors," Technical Report, DTIC, Fort Belvoir, Virginia (1985).
49. E. A. Gallie and P. A. Murtha, "Specific absorption and backscattering spectra for suspended minerals and chlorophyll-a in Chilko Lake, British Columbia," *Remote Sens. Environ.* **39**(2), 103–118 (1992).
50. Z.-P. Lee et al., "Diffuse attenuation coefficient of downwelling irradiance: an evaluation of remote sensing methods," *J. Geophys. Res.: Oceans* **110**(C2), C02017 (2005).
51. C. D. Mobley et al., "Comparison of numerical models for computing underwater light fields," *Appl. Opt.* **32**(36), 7484–7504 (1993).
52. D. M. Phillips and J. T. O. Kirk, "Study of the spectral variation of absorption and scattering in some Australian coastal waters," *Mar. Freshwater Res.* **35**(6), 635–644 (1984).
53. W. R. Bennett, "Spectra of quantized signals," *Bell Syst. Tech. J.* **27**(3), 446–472 (1948).
54. D. Sliney and M. Wolbarsht, *Safety with Lasers and Other Optical Sources*, Springer, New York (1980).
55. W. F. Royce, "Breeding habits of lake trout in New York," *Fish. Bull.* **52**, 59–76 (1951).
56. N. V. Martin, "Reproduction of lake trout in Algonquin Park, Ontario," *Trans. Am. Fish. Soc.* **86**(1), 231–244 (1957).
57. S. E. Deroche, "Observations on the spawning habits and early life of lake trout," *Prog. Fish-Cult.* **31**(2), 109–113 (1969).
58. M. Esteve, D. A. McLennan, and J. M. Gunn, "Lake trout (*Salvelinus namaycush*) spawning behaviour: the evolution of a new female strategy," *Environ. Biol. Fishes* **83**(1), 69–76 (2008).
59. A. M. Muir et al., "Lake charr *Salvelinus namaycush* spawning behaviour: new field observations and a review of current knowledge," *Rev. Fish Biol. Fish.* **22**(3), 575–593 (2012).
60. T. R. Binder et al., "New insight into the spawning behavior of lake trout, *Salvelinus namaycush*, from a recovering population in the Laurentian Great Lakes," *Environ. Biol. Fishes* **98**(1), 173–181 (2015).
61. D. T. Callaghan, P. J. Blanchfield, and P. A. Cott, "Lake trout (*Salvelinus namaycush*) spawning habitat in a northern lake: the role of wind and physical characteristics on habitat quality," *J. Great Lakes Res.* **42**, 299–307 (2016).
62. J. H. Churnside and P. A. McGillivary, "Optical properties of several pacific fishes," *Appl. Opt.* **30**(21), 2925–2927 (1991).
63. N. L. Seldomridge, J. A. Shaw, and K. S. Repasky, "Dual-polarization lidar using a liquid crystal variable retarder," *Opt. Eng.* **45**(10), 106202 (2006).
64. C. Cox and W. Munk, "Measurement of the roughness of the sea surface from photographs of the sun's glitter," *J. Opt. Soc. Am.* **44**(11), 838–850 (1954).
65. J. A. Shaw and J. H. Churnside, "Scanning-laser glint measurements of sea-surface slope statistics," *Appl. Opt.* **36**(18), 4202–4213 (1997).
66. G. C. Guenther, "Wind and nadir angle effects on airborne lidar water surface returns," in *1986 Technical Symp. Southeast*, pp. 277–286 (1986).
67. J. A. Shaw et al., "Airborne lidar mapping of invasive lake trout in Yellowstone Lake," in *Proc. of the 24th Int. Laser Radar Conf.*, Vol. 11, pp. 905–908 (2008).
68. J. H. Churnside and L. A. Ostrovsky, "Lidar observation of a strongly nonlinear internal wave train in the Gulf of Alaska," *Int. J. Remote Sens.* **26**(1), 167–177 (2005).
69. J. H. Churnside, J. J. Wilson, and V. V. Tatarskii, "Lidar profiles of fish schools," *Appl. Opt.* **36**(24), 6011–6020 (1997).
70. J. H. Churnside, D. A. Demer, and B. Mahmoudi, "A comparison of lidar and echosounder measurements of fish schools in the Gulf of Mexico," *ICES J. Mar. Sci.* **60**(1), 147–154 (2003).
71. R. W. Preisendorfer, "Secchi disk science: visual optics of natural waters," *Limnol. Oceanogr.* **31**(5), 909–926 (1986).

72. R. J. Davies-Colley and W. N. Vant, "Estimation of optical properties of water from Secchi disk depths," *J. Am. Water Resour. Assoc.* **24**(6), 1329–1335 (1988).
73. J. T. Kirk, *Light and Photosynthesis in Aquatic Ecosystems*, Cambridge University Press (1994).

**Michael R. Roddewig** is a PhD student of electrical engineering at Montana State University. He received his bachelor's degree from Michigan Tech in 2009 and his master's degree from Colorado School of Mines in 2012. He is a member of SPIE.

**Nathan J. Pust** received his bachelors degree in electrical engineering in 2002 and his PhD in electrical engineering from Montana State University in 2007. He is currently employed as a remote sensing and optical engineer for Tyvak Nano-Satellite Space Systems.

**James H. Churnside** is a researcher at the NOAA Earth System Research Laboratory, Boulder, Colorado, where he conducts research on development and applications of airborne lidar for oceanographic studies. He received his PhD in physics from Oregon Graduate Center, Beaverton, Oregon. He is a fellow of the OSA and SPIE.

**Joseph A. Shaw** is the director of the Optical Technology Center, professor of optics and photonics and of electrical and computer engineering, and affiliate professor of physics at Montana State University in Bozeman, Montana. He received his PhD and MS degrees in optical sciences from the University of Arizona, his MS degree in electrical engineering from the University of Utah, and his BS degree in electrical engineering from the University of Alaska–Fairbanks. He conducts research on the development and application of radiometric, polarimetric, and laser-based optical remote sensing systems. He is a fellow of the OSA and SPIE.